ARTICLE

Fluorescence Enhancement by Au Nanostructures: Nanoshells and Nanorods

Rizia Bardhan,[†,§] Nathaniel K. Grady,[‡,§] Joseph R. Cole,[‡,§] Amit Joshi,[∥] and Naomi J. Halas[†,‡,§,*]

[†]Department of Chemistry and [‡]Department of Electrical and Computer Engineering, [§]Laboratory for Nanophotonics, Rice University, Houston, Texas 77005, and [∥]Department of Radiology, Baylor College of Medicine, Houston, Texas 77005

ABSTRACT Metallic nanoparticles influence the quantum yield and lifetime of adjacent fluorophores in a manner dependent on the properties of the nanostructure. Here we directly compare the fluorescence enhancement of the near-infrared fluorophore IR800 by Au nanoshells (NSs) and Au nanorods (NRs), where human serum albumin (HSA) serves as a spacer layer between the nanoparticle and the fluorophore. Our measurements reveal that the quantum yield of IR800 is enhanced from ~7% as an isolated fluorophore to 86% in a NSs—HSA—IR800 complex and 74% in a NRs—HSA—IR800 complex. This dramatic increase in fluorescence shows tremendous potential for contrast enhancement in fluorescence-based bioimaging.

KEYWORDS: fluorescence enhancement · IR800 · gold nanoshells · gold nanorods · frequency domain lifetime decay

Fluorescence imaging has seen widespread use in clinical diagnosis and monitoring processes in biological systems.[1] The development of contrast agents, such as fluorescent probes with engineered biomarker functionalities, has become integral to the advancement of new bioimaging technologies.[2] Fluorescent molecules emitting at wavelengths in the physiologically relevant "water window" (700−900 nm) are of particular interest due to the large penetration depth of near-infrared (NIR) light in most biological media and offer the potential for imaging at significant depths in living tissues.[3] However, achieving bright fluorescent emission with photostable and biocompatible near-IR fluorophores has proven to be extremely difficult. It has long been known that, in the proximity of a metallic surface, fluorescence emission of molecules can be enhanced; this is also the case for metallic nanostructures and nanoparticles adjacent to a fluorophore.[4−7] The presence of a nearby metallic nanoparticle can not only enhance the quantum yield but also stabilize adjacent fluorophores against photobleaching, further enhancing their practical use in bioimaging applications.[8] In new and emerging light-assisted therapeutic applications such as photothermal cancer therapy, the addition of bright near-IR fluorescence to a therapeutic nanostructure complex could provide additional diagnostic imaging capabilities for this treatment strategy that could facilitate clinical use. Understanding precisely how metallic nanostructures enhance molecular fluorescence is of general fundamental interest and may ultimately provide practical routes to enhancing light emission from a variety of materials systems and devices far beyond the specific application of bioimaging.

Metal nanostructures exhibit remarkable optical properties due to excitation of their surface plasmons by incident light, which results in a significant enhancement of the electromagnetic field at the nanoparticle surface. This enhanced near field can be used to design highly sensitive chemical and biosensors with specific plasmon resonances tailored by the nanoparticle geometry.[9,10] Metallic nanoparticles have been shown to enhance the fluorescence emission and decrease the molecular excited-state lifetimes of vicinal fluorophores. The fluorescence enhancement is attributable to a combination of processes including enhanced absorption by the molecule, modification of the radiative decay rate of the molecule, and enhanced coupling efficiency of the fluorescent emission to the far field.[8,11]

The plasmon resonant properties of metallic nanoparticles can be controlled by optimizing the nanoparticle topology, dimensions, and composition.[12−15] When plasmonic nanoparticles are much smaller than a wavelength of light, they are absorbers, much like molecules. Nanoparticles larger than a few tens of nanometers both absorb and scatter light. While both the absorption and scattering cross sections of a

*Address correspondence to halas@rice.edu.

Received for review January 2, 2009 and accepted February 11, 2009.

Published online February 20, 2009.
10.1021/nn900001q CCC: $40.75

© 2009 American Chemical Society

plasmon resonant nanoparticle increase with increasing particle size, scattering begins to dominate in this larger-size regime.[16] Au nanorods (NRs) and Au nanoshells (NSs) are both particularly useful for biological applications since their near-field and far-field optical properties can be tuned controllably throughout the NIR water window by varying their geometry. For NRs, the aspect ratio defines two distinct plasmon resonance frequencies associated with the longitudinal and transverse dimensions of the nanostructure.[17] For NSs, symmetric spherical nanoparticles consisting of a dielectric core and a metal shell, the plasmon resonances are determined by the relative size of the core and the metal shell layer.[18] NSs can be fabricated both in a small size regime ($d \sim 50$ nm) using Au_2S/Au and sizes up to a micron in silica/Au core/shell structures, accessing near-IR resonances over a large size range.[16] NRs tuned to the same NIR plasmon resonance frequency as silica/Au NSs are significantly smaller in size than the corresponding nanoshell, resulting in a much smaller contribution of scattering to the overall extinction cross section. Studying fluorescence enhancement by these two types of structures allows us to examine how the properties of both nanostructures contribute to this effect.

We have recently shown that the fluorescence of NIR fluorophores can be significantly enhanced when the molecules are in close proximity to NSs.[6,7] Fluorescence enhancements as large as 50 fold were obtained when the plasmon resonance of the nanoshell was tuned to the emission wavelength of the fluorophore, for a nanoshell designed with a significant scattering cross section at that wavelength. In the study, we compare the fluorescence enhancement of the NIR fluorophore IR800 positioned a small, controlled distance from NSs and NRs. We quantified the fluorescence enhancement of IR800 experimentally by measuring the angle resolved scattering intensities, frequency domain fluorescence decay, and quantum yield of IR800 before and after binding to the nanoparticles. We also calculated the scattering cross sections of NSs and NRs to determine the scattering intensities of the nanoparticles and relative contribution of nanoparticle scattering toward molecular fluorescence enhancement.

When a fluorophore is adsorbed directly onto a metal surface, its fluorescence is quenched. However, at a distance of a few nanometers from the nanoparticle surface, the fluorescence can be strongly enhanced.[19] IR800 molecules were placed in close proximity of NSs and NRs surfaces by coating the nanoparticles with a 5−11 nm layer of human serum albumin (HSA) in order to prevent quenching of IR800. Serum albumin, a large multidomain protein relevant to many physiological functions,[20] has been conjugated to Au nanoparticles extensively for cell-targeting applications.[21,22] It binds to Au by electrostatic attraction between the amine groups of the protein and the negative charge on the gold surface or, alternatively, by

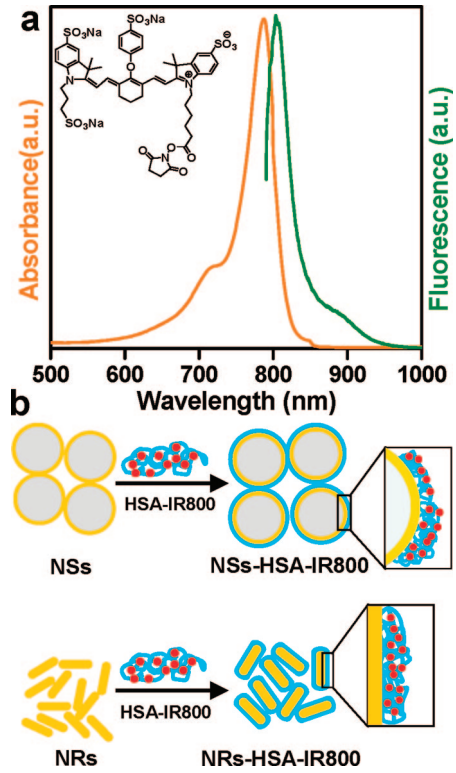

Figure 1. (a) Absorption−emission profile ($\lambda_{max\text{-}Ab} \sim 782$ nm and $\lambda_{max\text{-}Em} \sim 804$ nm) of IR800 conjugated with HSA. Chemical structure of IR800 is provided as an inset. (b) Schematic diagram illustrating the conjugation of HSA−IR800 protein−fluorophore complex to nanoshells (NSs) and nanorods (NRs) to form NSs−HSA−IR800 and NRs−HSA−IR800, respectively. The blue curved line represents HSA, and the red dots represent IR800 dye.

covalent attachment between the Au surface and amino acid functional groups present in the protein.[23] In this study, HSA acts as both a spacer layer as well as a linker of the fluorophore to the nanoparticle. It contains an abundance of α-amines at N-terminals and ε-amines on lysine side chains, which covalently bind to IR800 *via* the *N*-hydroxysuccinimide (NHS) ester group to form a stable protein−dye complex.[24] The NHS ester group facilitates protein conjugation, and the presence of the negatively charged sulfonate groups makes IR800 soluble in aqueous media. While these properties make IR800 a suitable dye for bioimaging,[25] it is limited by low quantum efficiency compared to commonly used visible dyes such as boron dipyrromethene (BODIPY) and fluorescein isothiocyanate (FITC). Therefore, by binding IR800 to metal nanoparticles with a suitably determined spacer layer, the quantum yield can be significantly enhanced.

RESULTS AND DISCUSSION

The absorption−emission profile of IR800 conjugated to HSA in sodium phosphate buffer (Na_3PO_4, pH $\sim$ 8.0) is shown in Figure 1a. The absorbance maximum of the protein−fluorophore complex is observed at 782 nm, and the fluorescence emission maximum at 804 nm. The IR800 molecules were conjugated to HSA

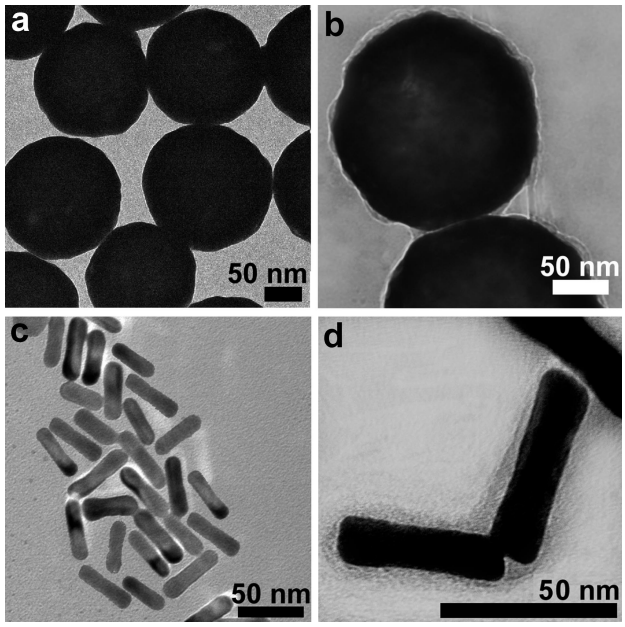

Figure 2. TEM micrographs of (a) NSs [r_1, r_2] = [63, 78] nm, (b) NSs coated with 8 ± 3 nm HSA−IR800, (c) NRs [w, l] = [11, 46] nm, and (d) NRs coated with 8 ± 3 nm HSA−IR800.

to form the HSA−IR800 complex, which was then bound to NSs (NSs−HSA−IR800) and NRs (NRs−HSA−IR800) as demonstrated in Figure 1b.

HSA−IR800 conjugation was performed at room temperature, and the protein−fluorophore complex was dialyzed for 24 h to remove excess dye (see Methods, section II). It was determined that approximately 16 molecules of IR800 were bound to each HSA molecule (see Methods, section V). The bioconjugation of the HSA−IR800 complex to the nanoparticles was performed in Na_3PO_4 buffer at room temperature and protected from light, and excess protein−fluorophore mixture was removed by centrifuging the nanoparticle conjugates in small aliquots (see Methods, section III). We determined that ~63 HSA−IR800 complexes were conjugated to each NS and ~4 HSA−IR800 complexes were bound to each NR (see Methods, section V). However, the total number of HSA−IR800 complexes bound to NSs or NRs was kept constant by adjusting the nanoparticle concentration, such that the total surface area available for conjugation was equivalent for both NSs and NRs (see Methods, section IV).

The geometry of the nanoparticles coated with HSA−IR800 was characterized with transmission electron microscopy (TEM). TEM micrographs of NSs with dimensions [r_1, r_2] = [63, 78] nm, where r_1 is the radius of the silica core and r_2 is the radius of the Au shell, are shown in Figure 2a. NRs, [w, l] = [11, 46] nm, where w is the width and l is the length, are shown in Figure 2c. The NSs and NRs coated with a uniform 8 ± 3 nm layer of HSA are shown in Figure 2b and Figure 2d, respectively.

The plasmon resonance of NSs and NRs shifts to longer wavelengths by 5−8 nm when HSA−IR800 is adsorbed, due to the higher refractive index of HSA than H_2O[26,27] (Supporting Information Figure S1). The plasmon resonances of the nanoparticles were tuned to the emission wavelength of the fluorophore−protein complex to maximize the fluorescence enhancement.[6] The extinction maximum of NSs−HSA−IR800 was observed at ~805 nm, and that of NRs−HSA−IR800 was observed at ~804 nm, as shown in Figure 3a. The corresponding emission spectra of HSA−IR800 conjugated to the nanoparticles are shown in Figure 3b. HSA−IR800 was used as the control sample rather than IR800 in aqueous solution to ensure that the fluorophore was in essentially the same chemical environment in all measurements. The emission spectra of NSs coated with HSA without IR800 and NRs coated with HSA without IR800 are also provided in the Supporting Information Figure S3. The nanoparticles exhibited negligible fluorescence in the near-infrared without the fluorophore. The reference sample as well as the nanoparticle conjugates were excited at 780 nm, and the fluorescence spectra were collected in solution under identical excitation and detection conditions, allowing direct comparison of the various nanoparticle−fluorophore complexes. A maximum fluorescence enhancement of ~40 was measured for NSs−HSA−IR800 relative to the control sample, and an enhancement of ~9 was found for NRs−HSA−IR800. The emission spectra of the fluorophore−nanoparticle conjugates excited at 720 nm are also provided in the Supporting Information Figure S4. No notable difference in the line shape of the emission spectra of IR800 in the presence or absence of the nanostructures was observed either for excitation at 720 nm or for excitation at 780 nm.

Since the nanoparticles used in this experiment vary in size, their relative scattering cross sections also differ significantly, which directly affects their fluorescence enhancement efficiency. We determined the scattering intensities of the NSs and NRs by calculating their scattering cross sections

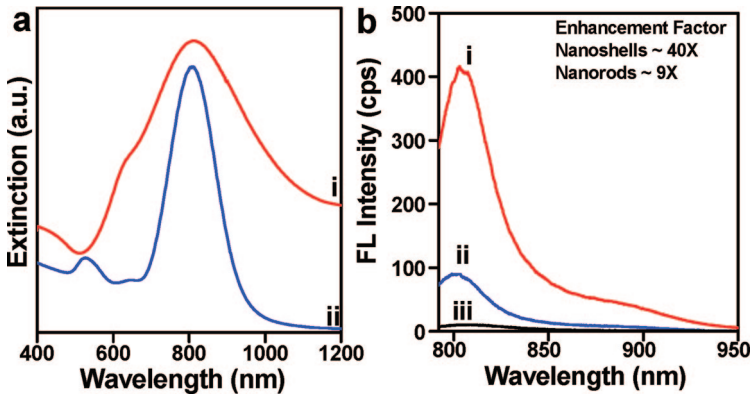

Figure 3. (a) Extinction spectra of (i) NSs−HSA−IR800, λ_{max} ~ 805 nm, and (ii) NRs−HSA−IR800, λ_{max} ~ 804 nm are shown. Spectra are offset for clarity. (b) Fluorescence (FL) spectra, λ_{max} ~ 804 nm of (i) NSs−HSA−IR800, (ii) NRs−HSA−IR800, and (iii) control sample HSA−IR800 are shown.

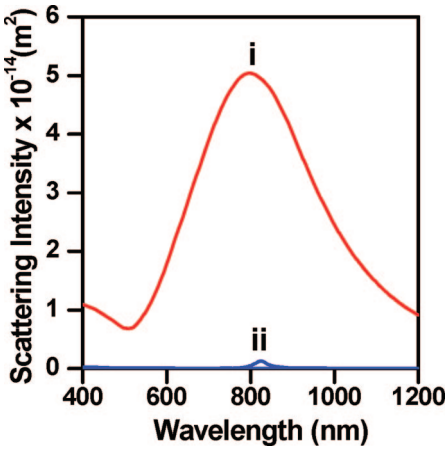

Figure 4. Calculated scattering spectra of (i) NSs [r_1, r_2] = [63, 78] nm, $\lambda_{max\text{-}scattering}$ observed at 800 nm and (ii) NRs [w, l] = [11, 46] nm, $\lambda_{max\text{-}scattering}$ observed at 824 nm.

using experimentally obtained nanoparticle sizes. The calculated scattering intensities for NSs [r_1, r_2] = [63, 78] nm in aqueous medium were obtained using Mie theory, and the maximum plasmon resonance peak was observed at 800 nm. The theoretical scattering intensity of NRs was calculated by using the finite element method (FEM) (as implemented by COMSOL Multiphysics). The nanorods were modeled as cylindrical objects with hemispherical end-caps in H_2O, estimating size obtained from TEM [w, l] = [11, 46] nm. The dielectric function used for Au was obtained from literature values.[28] The calculated longitudinal plasmon mode of NRs showed a maximum at a wavelength of 824 nm in water. The experimentally observed longitudinal plasmon resonance of NRs (804 nm) differs from that calculated theoretically because the energy of the longitudinal mode depends strongly on the end-cap geometry.[29] Nonetheless, the calculated scattering spectra shown in Figure 4 indicate that NSs scatter more efficiently than NRs for the sizes of nanoparticles studied.

Experimentally we observed ~34 times stronger scattering from NSs compared to NRs at 785 nm by measuring angular scattering distribution (Supporting Information Figure S2b). The larger scattering efficiency of NSs relative to NRs studied here correlates with the larger fluorescence enhancement observed for IR800 by NSs.

In addition to the scattering characteristics of the nanoparticles, increasing the radiative decay rate of the fluorophore contributes substantially to fluorescence enhancement. In a homogeneous solution, fluorophores emit light into free space and are observed in the far field. The observed emission of the fluorophore in the absence of any quenching interactions is described in terms of quantum yield (Q_0) and lifetime (τ_0). The quantum yield, given by

$$Q_0 = \frac{\Gamma}{\Gamma + k_{nr}} \quad (1)$$

is the fraction of the excited fluorophores which relaxes by radiative decay (Γ) relative to the total relaxation rate ($\Gamma + k_{nr}$). The observed lifetime is simply the inverse of the total decay rate of the excited state:

$$\tau_0 = \frac{1}{\Gamma + k_{nr}} \quad (2)$$

When a fluorophore is in the presence of a metal nanoparticle, the enhanced near field of the nanoparticle increases the amount of light absorbed by the molecule. In addition, electromagnetic coupling occurs between the fluorophore and the nanoparticle plasmon, causing an increase in the radiative decay rate of the molecule at the emission wavelength by a factor γ_r. As a result, the effective radiative decay rate is equivalent to $\gamma_r\Gamma$. The modified quantum yield (Q_M) and lifetime (τ_M) are then given by

$$Q_M = \frac{\gamma_r\Gamma}{\gamma_r\Gamma + k_{nr}} \quad (3)$$

$$\tau_M = \frac{1}{\gamma_r\Gamma + k_{nr}} \quad (4)$$

We assume that the nonradiative decay rate, k_{nr}, is unaffected by the presence of the nanoparticles.

The change in radiative lifetime for IR800 conjugated to NSs and NRs *via* HSA was determined experimentally by monitoring the frequency domain fluorescence decay in aqueous solution. The lifetime spectra of IR800, HSA−IR800, NRs−HSA−IR800, and NSs−HSA−IR800 are shown in Figure 5. The intrinsic lifetime of the fluorophore was measured to be ~564 ps, which corresponds well to the previously reported value.[25] The lifetime decreased to 427 ps when IR800 molecules were bound to HSA (Figure 5b). This is due to a small enhancement in quantum yield of the fluorophore when conjugated to the protein, attributable to an increased steric stabilization of IR800 bound to HSA. This reduces the mobility of the fluorophore in aqueous solution, resulting in higher stability and a decreased lifetime.[30] The lifetime of IR800 bound to the nanoparticles *via* HSA was reduced significantly to 121 ps for NRs−HSA−IR800 and 68 ps for NSs−HSA−IR800. These measured lifetimes confirm the theoretical prediction of enhanced quantum yield and diminished lifetime of fluorophores near metallic surfaces.[7]

In the frequency domain technique, lifetime measurements are obtained by exciting the fluorescent sample with intensity-modulated light at a high frequency comparable to τ^{-1} of the sample. Subsequent to excitation, the fluorescence emission of the sample follows the same modulation frequency as the excitation, but it is delayed in time relative to the excitation.

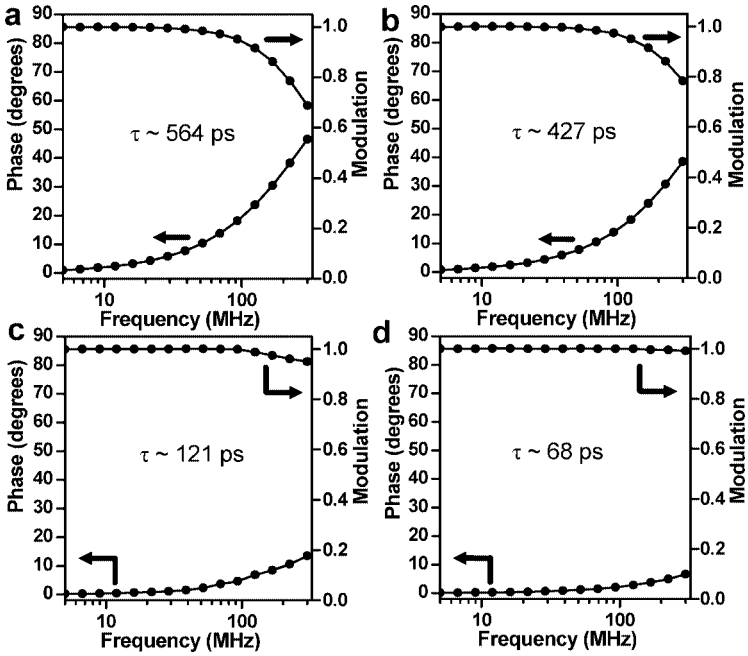

Figure 5. Frequency domain fluorescence decay of (a) IR800 ($\tau \sim 564$ ps), (b) HSA−IR800 ($\tau \sim 427$ ps), (c) NRs−HSA−IR800 ($\tau \sim 121$ ps), and (d) NSs−HSA−IR800 ($\tau \sim 68$ ps). The curves referring to phase and modulation are shown with arrows.

The time delay is measured as a phase shift (Φ) from which the lifetime (τ_Φ) is determined:

$$\tau_\Phi = \frac{1}{\omega}\tan(\Phi) \qquad (5)$$

where ω is angular frequency. The fluorescence lifetime data can be evaluated in terms of a single exponential (SE) model or a multiexponential (ME) model. A SE model is appropriate for samples consisting of a single fluorophore in a homogeneous environment, while a ME model describes the fractional contribution of decay time for each component present in a sample mixture.[31] The ME model for analyzing the intensity decay is given by

$$I(t) = \sum_i \alpha_i e^{\frac{-t}{\tau_i}} \qquad (6)$$

where τ_i are observed lifetimes with amplitude or molecular fraction α_i, such that

$$\sum_i \alpha_i = 1$$

The amplitude-weighted lifetime is then

$$\langle\tau\rangle = \sum_i \alpha_i \tau_i \qquad (7)$$

The results of fitting to a ME decay analysis are represented in Table 1. The decay rate for IR800 in aqueous media, in the absence of any other component in the solution, fits a SE decay model. However, the HSA−IR800 complex required a ME decay model, demonstrating that two different environments are available to the fluorophore with distinct lifetimes in each individual environment. About 90% of the IR800 molecules were covalently attached to HSA with a fluorescence decay of 418 ps. The lifetime of the remaining fraction was similar to that observed for free IR800 in aqueous media, suggesting that a small fraction of unbound fluorophores remain in the HSA−IR800 solution. The ME analysis of the fluorescence decay of IR800 conjugated to nanoparticles indicates three distinct environments, which we interpret as IR800 molecules conjugated to the nanoparticle−HSA, IR800 molecules bound to HSA only, and the free fluorophore in solution. Most of the fluorophores in these samples exhibited a significantly reduced lifetime, indicating that nearly all of the dye molecules were attached to the nanoparticles *via* the HSA layer. This analysis reveals that both nanoparticle samples had less than 2% of unbound HSA−IR800 complex and less than 1% of free fluorophore in the solution mixture. This is attributable to the high affinity of the protein for Au nanoparticle surface as well as the use of a fluorophore with a chemical linker which can covalently attach to the protein. Therefore, the nanoparticle−HSA−IR800 system provides a useful complex for determining individual lifetime components. The χ^2_R values shown in the last column of Table 1 are the goodness of fit parameter, obtained by fitting calculated values to experimentally obtained parameters by a nonlinear least-squares deconvulation method. The χ^2_R values represented here are within 5−10% of the random deviations in the data.[31]

In order to determine the radiative rate enhancement from the experimentally measured changes in lifetime, the nonradiative decay rate must be known. By combining and rearranging eqs 1 and 2, the radiative and nonradiative decay rate can be experimentally obtained from the lifetime and quantum yield:

TABLE 1. Multiexponential Analysis of Intensity Decay of IR800 with Nanoparticles Showing Molecular Fraction (α), Observed Lifetime (τ_i, ns), Amplitude-Weighted Lifetime ($\langle\tau\rangle$, ns), and Goodness of Fit Parameter (χ^2_R)

sample	α_i	τ_i	$\langle\tau\rangle$	χ^2_R
	1	0.564		
IR800	—	—	0.564	1.57
	—	—		
HSA-IR800	0.076	0.547		
	0.924	0.418	0.427	1.54
	—	—		
NRs-HSA-IR800	0.008	0.550	0.121	1.42
	0.019	0.419		
	0.973	0.112		
NSs-HSA-IR800	0.005	0.568	0.068	1.39
	0.01	0.421		
	0.985	0.065		

$$\Gamma = \frac{Q_0}{\tau_0} \quad (8)$$

$$k_{nr} = \frac{1}{\tau_0} - \Gamma \quad (9)$$

The quantum yield of IR800 (Q) was determined experimentally using indocyanine green (ICG) as a reference sample with a known quantum yield (Q_R) of ~1% in aqueous media.[32] The NIR excitation−emission profile of ICG (excitation = 780 nm, emission = 820 nm) is similar to that of IR800 and is therefore ideal as a reference sample for quantum yield determination. The quantum yield was computed by measuring the optical density of solutions with equivalent concentrations of IR800 (OD) and ICG (OD_R) and by calculating the integrated fluorescence intensity of IR800 (I) and ICG (I_R):

$$Q = Q_R \frac{I}{I_R} \frac{OD}{OD_R} \frac{\eta}{\eta_R} \quad (10)$$

where η is the refractive index of sample medium and η_R is the refractive index of the reference medium, which are equivalent in this experiment ($\eta = \eta_R = \eta_{H_2O} = 1.33$). By using eq 10, the quantum yield of IR800 was determined to be 7% in H_2O, and that of the HSA−IR800 complex was determined to be 11%. Using the quantum yield and lifetime measured independently, eqs 8 and 9 allow determination of the radiative and nonradiative decay rates of the fluorophore as shown in Table 2. The quantum yield values obtained for IR800 in aqueous media as well as HSA−IR800 are comparable to those reported in the literature.[33]

The radiative rate enhancement of IR800 induced by NSs and NRs and the improved quantum yields can now be calculated by rearranging eqs 3 and 4:

$$\gamma_r \Gamma = \frac{1}{\tau_M} - k_{nr} \quad (11)$$

$$Q_M = \gamma_r \Gamma \cdot \tau_M \quad (12)$$

where τ_M is obtained from Table 1, and k_{nr} is the nonradiative decay rate for HSA−IR800. We assume that k_{nr} is unaltered from HSA−IR800 for both NSs−HSA−IR800 and NRs−HSA−IR800 complexes because no fluorescence quenching was observable and the chemical environment of the fluorophore was equivalent in all cases. The nonradiative decay rate does increase when the chemical environment of the fluorophore is changed[34] from solution phase to being bound to HSA. Table 2 shows that the k_{nr} increases when IR800 is bound to HSA compared to the free fluorophore in solution. On a metallic surface, the nonradiative decay rate also increases for short fluorophore−metal distances, <4 nm,[35,36] since the nonradiative energy transfer rate depends on the inverse cube of the molecule−surface separation.[35] However, in our nanostructure complexes, HSA provides a spacer layer of ~8 nm between the fluorophore and the metal nanoparticle surface. For this significantly larger metal−molecule distance, a significant increase in k_{nr} due to the metal nanoparticle is not anticipated.[6,7] Therefore we assume that k_{nr} is essentially the same for HSA−IR800 in solution and for HSA−IR800 adsorbed sequentially onto a nanoshell or nanorod surface. The radiative decay rates of NRs−HSA−IR800 and NSs−HSA−IR800 and the quantum efficiencies are also shown in Table 2. The high quantum yield of 86% for NSs−HSA−IR800 demonstrates that plasmonic enhancement can be used to create NIR-fluorescent species with similar intensities as visible dyes. Although the NRs achieve a lower quantum yield of 74% due to the lower scattering efficiency of the particles, this is still a very high value for a NIR fluorophore, and these structures would certainly also be useful as markers in fluorescence-based bioimaging where the smaller physical size of the NRs-based nanoparticle complex would be desired.

TABLE 2. Quantum Yield (QY), Radiative Decay Rate (Γ), and Nonradiative Decay Rate (k_{nr}) of IR800, HSA−IR800, and HSA−IR800 with Nanoparticles

sample	QY	Γ	k_{nr}
IR800	0.07	1.241×10^8	1.648×10^9
HSA−IR800	0.11	2.576×10^8	2.084×10^9
NRs−HSA−IR800	0.74	6.180×10^9	2.084×10^9
NSs−HSA−IR800	0.86	1.262×10^{10}	2.084×10^9

The precise relative contribution of each process responsible for IR800 fluorescence enhancement, including absorption enhancement, scattering enhancement, and radiative decay rate enhancement, is difficult to determine since these processes are interdependent. Nevertheless, for the experimental parameters and nanoparticle geometries discussed here, the scattering efficiency of a nanoparticle appears to provide the most important mechanism for improving the quantum yield of a fluorophore. NRs predominantly enhance the emission of the fluorophore by absorption enhancement, owing to the high-intensity near field resulting from the longitudinal plasmon resonance. However, due to the significant difference in scattering cross sections of NSs and NRs, it is apparent that NSs increase the coupling efficiency of the fluorescence emission to the far field more efficiently than NRs. This explains the 40-fold fluorescence enhancement observed for IR800 bound to NSs compared to the 9-fold enhancement for IR800 bound to NRs. The radiative decay rate enhancement of the fluorophore is dependent on both the scattering efficiency as well as the absorption efficiency of nanoparticles. This explains why NRs enhance the quantum yield of IR800 by 74% as well as decrease the fluorophore's lifetime considerably.

CONCLUSIONS

In conclusion, we have examined the fluorescence enhancement of IR800 conjugated to NSs and NRs,

and we have shown that both NSs and NRs lead to large increases in quantum yield relative to the isolated fluorophore. We have observed that NSs are more efficient in improving the emissive properties of a fluorophore due to their significant scattering cross section at the emission wavelength of the fluorophore. Additionally, the near-field response of NSs gives rise to a considerable enhancement in the absorption and the radiative decay rate of IR800, resulting in 40-fold enhancement and 86% quantum yield. IR800 molecules bound to NRs demonstrate a 9-fold emission enhancement and a 74% quantum yield, attributable to the high local field enhancement at the longitudinal plasmon wavelength. Utilizing Au nanoparticles with appropriate geometry and dimensions for emission enhancement is a useful strategy for enhancing the detection sensitivity of low-quantum-yield fluorescent emitters. This approach is also potentially valuable in biomedical imaging and, moreover, can be conveniently generalized to enhance other fluorescent media.

METHODS

Section I. Nanoparticle Fabrication. All chemicals were purchased from Sigma Aldrich, and IR800 NHS ester was purchased from Licor Biosceinces. Au nanoshells (NSs) $[r_1, r_2] = [63, 78]$ nm were fabricated by seed-mediated electroless plating of Au onto silica spheres as previously reported.[37] Briefly, monodisperse silica nanospheres of 63 ± 2 nm radii were synthesized by the hydrolysis of tetraethylorthosilicate (TEOS) in basic solution *via* the Stöber method[38] and functionalized with (3-aminopropyl) triethoxysilane (APTES) overnight. These amine-terminated silica nanospheres were decorated with small gold colloid (2−3 nm) prepared by the method reported by Duff *et al.*[39] A continuous gold shell is grown around the silica nanospheres by reducing gold from a 1% solution of $HAuCl_4$ onto the attached small colloid in the presence of formaldehyde. The fabricated NSs were centrifuged several times and finally redispersed in sodium phosphate buffer (Na_3PO_4, pH ~ 8.0).

Au nanorods (NRs) $[w, l] = [11, 46]$ nm were fabricated by the method reported by Murphy and co-workers.[40] Briefly, the seed solution was prepared by gently mixing 7.5 mL of 0.1 M cetyltrimethylammonium bromide (CTAB) with 0.25 mL of 0.01 M $HAuCl_4$; 0.6 mL of ice-cold 0.01 M $NaBH_4$ was injected into the solution and mixed rapidly. The solution turns from a golden yellow color to a pale brown color. It is essential that the temperature of $NaBH_4$ is maintained at ~0 °C prior to mixing with CTAB and $HAuCl_4$ for proper growth of nanorods. The seed solution was then stored at 27 °C until further use. The growth solution was prepared by gently mixing 47.5 mL of 0.1 M CTAB, 2 mL of 0.01 M $HAuCl_4$, 0.3 mL of 0.01 M $AgNO_3$, and 0.32 mL of 0.1 M ascorbic acid in the order mentioned. Addition of ascorbic acid turns the solution from golden yellow to colorless; 0.25 mL of the seed solution was added to the growth solution and mixed gently, and then the solution was stored at 27 °C for 3 h without agitation. Within 20 min, the solution changes from colorless to pink and eventually changes to dark pinkish brown after 3 h. The NRs were washed twice at 8000 rpm to remove excess CTAB and finally redispersed in 10 mL of Na_3PO_4 buffer.

Section II. Protein and Fluorophore Conjugation. HSA was conjugated to IR800 by mixing equal volumes of 5 μM HSA aqueous solutions in Na_3PO_4 buffer and 30 μM IR800 aqueous solution at room temperature for 5 h, in the dark. The protein−flurophore complex was then dialyzed in Na_3PO_4 buffer for 24 h at room temperature protected from light, in a 3500 MW dialysis bag (MW of HSA is 67 kDA and MW of IR800 is 1166 g/mol) to remove excess dye. Absorbance peaks of the protein−dye complex (λ_{max} = 782 nm) and protein (λ_{max} = 280 nm) were monitored to account for free-dye removal. After sufficient removal of unbound dye, the ratio of fluorophore to protein concentration (N_{IR800}/NHSA) of the complex is determined by utilizing the absorbance of fluorophore at 782 nm (A_{IR800}), molar extinction coefficient of IR800 (ε_{IR800}), absorbance of HSA at 280 nm (A_{HSA}), molar extinction coefficient of HSA (ε_{HSA}) given by

$$N_{IR800}/N_{HSA} = [A_{IR800}/\varepsilon_{IR800}]/[A_{HSA}/\varepsilon_{HSA}]$$

where $\varepsilon_{IR800} = 240\,000\ M^{-1}\ cm^{-1}$ and $\varepsilon_{HSA} = 42\,864\ M^{-1}\ cm^{-1}$. The final protein concentration was calculated using the molecular weight (MW_{HSA}) and dilution factor (df) of original solution given by

$$N_{HSA} = [A_{HSA}/\varepsilon_{HSA}] \times MW_{HSA} \times df$$

The final protein concentration was ~4 μM, and fluorophore concentration was ~10 μM.

Section III. Protein−Fluorophore Complex Binding to Nanoparticles. The protein−fluorophore complex obtained was conjugated to the nanoparticles by adding 1 mL of HSA−IR800 solution in Na_3PO_4 buffer to 10 mL nanoshells and 10 mL nanorods dispersed in Na_3PO_4 buffer, respectively, under constant stirring. After 7 h conjugation at room temperature, in the dark, the nanoparticles were centrifuged in small aliquots of 500 μL to remove excess dye and resuspended in Na_3PO_4 buffer. The absorbance of the supernatant was closely monitored to account for unbound fluorophore concentration in the supernatant (9.55−9.65 μM). The concentration of the supernatant was then subtracted from the initial concentration of HSA−IR800, which was added to the nanoparticles to calculate the amount of HSA−IR800 on the nanoparticles. The final NSs concentration after resuspension in buffer was at ~10^8 particles/mL, and final NRs concentration was at ~10^9 particles/mL. The surface area available for the HSA−IR800 complex to bind to the nanoparticles was normalized (see below), and hence the concentration of fluorophore was equivalent for both the NSs−HSA−IR800 and NRs−HSA−IR800, ~400 ± 50 nM.

Instrumentation and Modeling. The nanoparticles were characterized by obtaining transmission electron microscope (TEM) images using a JEOL JEM-2010 TEM and absorbance measurements using a Varian Cary 5000 UV−vis−NIR spectrometer. Fluorescence emission spectra and frequency domain lifetime measurements were obtained using Jobin Yvon Fluorolog 3, and the samples were excited at 780 nm. The dynamic range of the Fluorolog 3 for lifetime measurements is 0−300 MHz. Angular scattering distribution was obtained using an in-house angle-resolved fluorescence emission apparatus.

The theoretical scattering intensity of NRs was calculated by using the finite element method (FEM) (as implemented by COMSOL Multiphysics).

Section IV. Calculation of Surface Area Available for Protein−Dye Complex To Bind to Nanoparticles. The amount of protein and fluorophore bound to the nanoparticles was quantified by assuming that IR800 binds to HSA similarly for both NSs and NRs. The available surface area for fluorophore binding is kept equivalent for both nanoparticle solutions. The concentration (C_{NS}) and extinction coefficient (σ_{NS}) for NSs were calculated utilizing Mie theory:

$$\sigma_{NS} = 9.6072 \times 10^{-10}\ cm^2 \quad \text{for NSs } [r_1, r_2] = [63, 78]\ nm$$

$$\begin{aligned} C_{NS} &= \ln(10) \times \text{absorbance}/\sigma \times \text{cuvette path length} \\ &= 2.303 \times 0.052/9.6072 \times 10^{-10}\ cm^2 \times 1\ cm \\ &= 1.25 \times 10^8\ \text{particles/mL} \end{aligned}$$

the surface area of one NS (SA_{NS}) $= 4\pi[r_2^2 - r_1^2] = 2.855 \times 10^{-14}\ m^2$

the surface area of NSs solution $= (SA_{NS}) \times C_{NS} = 3.568 \times 10^{-6}\ m^2/mL$

The extinction coefficient (σ_{NR}) for NRs [w, l] = [11, 46] nm resonant at ~800 nm has been reported previously as $\sigma_{NR} \sim 4 \times 10^{-11}\ cm^2$.[41] The concentration of NRs (C_{NR}) were calculated utilizing Gan's theory:

$$C_{NR} = 2 \times \text{absorbance}/\sigma \times \text{cuvette path length}$$
$$= 2 \times 0.043/4 \times 10^{-11}\ cm^2 \times 1\ cm$$
$$= 2.154 \times 10^9\ \text{particles/mL}$$

the surface area of one NR (SA_{NR}) $= 2\pi r^2 + 2\pi r l = 1.727 \times 10^{-15}\ m^2$

the surface area of NRs solution $= (SA_{NR}) \times C_{NR} = 3.719 \times 10^{-6}\ m^2/mL$

However, experimentally, the available nanoparticle surface area for fluorophore binding would vary slightly due to nonuniform size distribution of nanoparticles in solution.

Section V. Calculation of Number of Protein−Fluorophore Molecules Bound to the Nanoparticles. The diameter of a HSA molecule is approximately ~8 ± 3 nm, and we assume the diameter of a IR800 molecule is roughly ~2 nm, resulting in a hydrodynamic diameter of ~12 nm for the protein−fluorophore complex. We have determined the number of fluorophore molecules per protein molecule by taking a ratio of their surface area:

the surface area of one HSA molecule (SA_{HSA}) $= 4\pi r^2 = 4\pi(4 \times 10^{-9})^2 = 2.011 \times 10^{-16}\ m^2$

the surface area of one IR800 molecule (SA_{IR800}) $= 4\pi(1 \times 10^{-9})^2 = 1.256 \times 10^{-17}\ m^2$

the no. of IR800 molecules per HSA molecule $= SA_{HSA}/SA_{IR800} \approx$ 16 dye molecules

We have also calculated the number of molecules of protein−fluorophore complex per nanoparticle, for both NSs as well as NRs:

the surface area of one HSA−IR800 molecule ($SA_{HSA-IR800}$) $= 4\pi(6 \times 10^{-9})^2 = 4.523 \times 10^{-16}\ m^2$

the no. of HSA−IR800 molecules per NS $= SA_{NS}/SA_{HSA-IR800}$
$= 2.855 \times 10^{-14}\ m^2/4.523 \times 10^{-16}\ m^2$
$\approx$ 63 HSA−IR800 molecules

the no. of HSA−IR800 molecules per NR $= SA_{NR}/SA_{HSA-IR800}$
$= 1.727 \times 10^{-15}\ m^2/4.523 \times 10^{-16}\ m^2$
$\approx$ 4 HSA−IR800 molecules

However, as described above, the surface area available for the HSA−IR800 complex to bind to NSs and NRs has been normalized by adjusting the nanoparticle concentration. This provides almost equivalent amounts of protein−dye molecules to bind to each nanoparticle suspension.

Acknowledgment. We gratefully acknowledge the Robert A. Welch Foundation (C-1220), Air Force Office of Scientific Research Grant (F49620-03-C-0068), and Multidisciplinary University Research Initiative (W911NF-04-01-0203) for financial support. We thank Prof. Bruce Johnson, Lisa Brown, Britt Lassiter, Nikolay Mirin, and Surbhi Lal for helpful discussions, Rebekah Drezek for fluorescence emission measurements, and Eva M. Sevick-Muraca for lifetime measurements.

Supporting Information Available: Spectra showing plasmon resonance shift when nanoparticles are coated with HSA−IR800; schematic diagram of home-built angle-resolved fluorescence emission apparatus; angle-resolved scattering spectra of NSs and NRs; fluorescence spectra of control: nanostructures without fluorophore; fluorescence spectra of nanostructure−fluorophore conjugates excited at 720 nm. This material is available free of charge *via* the Internet at http://pubs.acs.org.

REFERENCES AND NOTES

1. Hillman, E. M. C.; Moore, A. All-Optical Anatomical Co-registration for Molecular Imaging of Small Animals Using Dynamic Contrast. *Nat. Photonics* **2007**, *1*, 526–530.
2. Kovar, J. L.; Simpson, M. A.; Schutz-Geschwender, A.; Olive, D. M. A Systematic Approach to the Development of Fluorescent Contrast Agents for Optical Imaging of Mouse Cancer Models. *Anal. Biochem.* **2007**, *367*, 1–12.
3. Weissleder, R. A Clearer Vision For *in vivo* Imaging. *Nat. Biotechnol.* **2001**, *19*, 316–317.
4. Anger, P.; Bharadwaj, P.; Novotny, L. Enhancement and Quenching of Single-Molecule Fluorescence. *Phys. Rev. Lett.* **2006**, *96*, 1130021–1130024.
5. Drexhage, K. H. Influence of a Dielectric Interface On Fluorescence Decay Time. *J. Lumin.* **1970**, *1*, 693–701.
6. Tam, F.; Goodrich, G. P.; Johnson, B. R.; Halas, N. J. Plasmonic Enhancement of Molecular Fluorescence. *Nano Lett.* **2007**, *7*, 496–501.
7. Bardhan, R.; Grady, N. K.; Halas, N. J. Nanoscale Control of Near-Infrared Fluorescence Enhancement Using Au Nanoshells. *Small* **2008**, *4*, 1716–1722.
8. Lakowicz, J. R. Radiative Decay Engineering 5: Metal-Enhanced Fluorescence and Plasmon Emission. *Anal. Biochem.* **2005**, *337*, 171–194.
9. Anker, J. N.; Hall, W. P.; Lyandres, O.; Shah, N. C.; Zhao, J.; Van Duyne, R. P. Biosensing With Plasmonic Nanosensors. *Nat. Mater.* **2008**, *7*, 442–453.
10. Liao, H.; Nehl, C. L.; Hafner, J. H. Biomedical Applications of Plasmon Resonant Metal Nanoparticles. *Nanomedicine* **2006**, *1*, 201–208.
11. Chance, R. R.; Prock, A.; Silbey, R. Lifetime of an Emitting Molecule Near a Partially Reflecting Surface. *J. Chem. Phys.* **1974**, *60*, 2744–2748.
12. Wang, H.; Brandl, D. W.; Nordlander, P.; Halas, N. J. Plasmonic Nanostructures: Artificial Molecules. *Acc. Chem. Res.* **2007**, *40*, 53–62.
13. Lee, K. S.; El-Sayed, M. A. Gold and Silver Nanoparticles in Sensing and Imaging: Sensitivity of Plasmon Response to Size, Shape, and Metal Composition. *J. Phys. Chem. B* **2006**, *110*, 19220–19225.
14. Hao, F.; Nehl, C. L.; Hafner, J. H.; Nordlander, P. Plasmon Resonances of a Gold Nanostar. *Nano Lett.* **2007**, *7*, 729–732.
15. Wang, H.; Goodrich, G. P.; Tam, F.; Oubre, C.; Nordlander, P.; Halas, N. J. Controlled Texturing Modifies the Surface Topography and Plasmonic Properties of Au Nanoshells. *J. Phys. Chem. B* **2005**, *109*, 11083–11087.
16. Tam, F.; Chen, A. L.; Kundu, J.; Wang, H.; Halas, N. J. Mesoscopic Nanoshells: Geometry-Dependent Plasmon Resonances Beyond the Quasistatic Limit. *J. Chem. Phys.* **2007**, *127*, 204703.
17. Nikoobakht, B.; El-Sayed, M. A. Preparation and Growth Mechanism of Gold Nanorods (NRs) Using Seed-Mediated Growth Method. *Chem. Mater.* **2003**, *15*, 1957–1962.
18. Prodan, E.; Radloff, C.; Halas, N. J.; Nordlander, P. Hybridization Model for the Plasmon Response of Complex Nanostructures. *Science* **2003**, *302*, 419–422.
19. Sokolov, K.; Chumanov, G.; Cotton, T. M. Enhancement of Molecular Fluorescence near the Surface of Colloidal Metal Films. *Anal. Chem.* **1998**, *70*, 3898–3905.

20. He, X. M.; Carter, D. C. Atomic Structure and Chemistry of Human Serum Albumin. *Nature* **1992**, *358*, 209–215.
21. Tkachenko, A. G.; Xie, H.; Liu, Y.; Coleman, D.; Ryan, J.; Glomm, W. R.; Franzen, S.; Feldheim, D. L. Cellular Trajectories of Peptide-Modified Gold Particle Complexes: Comparison of Nuclear Localization Signals and Peptide Transduction Domains. *Bioconjugate Chem.* **2004**, *15*, 482–490.
22. Rosi, N. L.; Mirkin, C. A. Nanostructures in Biodiagnostics. *Chem. Rev.* **2005**, *105*, 1547–1562.
23. Brewer, S. H.; Glomm, W. R.; Johnson, M. C.; Knag, M. K.; Franzen, S. Probing BSA Binding to Citrate-Coated Gold Nanoparticles and Surfaces. *Langmuir* **2005**, *21*, 9303–9307.
24. Patel, N.; Davies, M. C.; Heaton, R. J.; Roberts, C. J.; Tendler, S. J. B.; Williams, P. M. A Scanning Probe Microscopy Study of the Physisorption and Chemisorption of Protein Molecules onto Carboxylate Terminated Self-Assembled Monolayers. *Appl. Phys. A: Mater. Sci. Process.* **1998**, *66*, S569–S574.
25. Houston, J. P.; Ke, S.; Wang, W.; Li, C.; Sevick-Muraca, E. M. Quality Analysis of in vivo Near-Infrared Fluorescence and Conventional Gamma Images Acquired Using a Dual-Labeled Tumor-Targeting Probe. *J. Biomed. Opt.* **2005**, *10*, 0540101–05401011.
26. Prodan, E.; Lee, A.; Nordlander, P. The Effect of a Dielectric Core and Embedding Medium on the Polarizability of Metallic Nanoshells. *Chem. Phys. Lett.* **2002**, *360*, 325–332.
27. Link, S.; Mohamed, M. B.; El-Sayed, M. A. Simulation of the Optical Absorption Spectra of Gold Nanorods as a Function of Their Aspect Ratio and the Effect of the Medium Dielectric Constant. *J. Phys. Chem. B* **1999**, *103*, 3073–3077.
28. Johnson, P. B.; Christy, R. W. Optical Constants of the Noble Metals. *Phys. Rev. B* **1972**, *6*, 4370–4379.
29. Prescott, S. W.; Mulvaney, P. Gold Nanorod Extinction Spectra. *J. Appl. Phys.* **2006**, *99*, 1235041–1235047.
30. Valdes-Aguilera, O.; Cincotta, L.; Foley, J.; Kochevar, I. E. Photobleaching of a Cyanine Dye in Solution and in Membranes. *Photochem. Photobiol.* **1987**, *45*, 337–344.
31. Lakowicz, J. R. Time-Domain Lifetime Measurements. In *Principles of Fluorescence Spectroscopy*, 2nd ed.; Kluwer Academic/Plenum: New York, 1999; pp 95−184.
32. Soper, S. A.; Mattingly, Q. L. Steady-State and Picosecond Laser Fluorescence Studies of Nonradiative Pathways in Tricarbocyanine Dyes: Implications to the Design of Near-IR Fluorochromes with High Fluorescence Efficiencies. *J. Am. Chem. Soc.* **1994**, *116*, 3144–3152.
33. Ohnishi, S.; Lomnes, S. J.; Laurence, R. G.; Gogbashian, A.; Mariani, G.; Frangioni, J. V. Organic Alternatives to Quantum Dots for Intraoperative Near-Infrared Fluorescent Sentinel Lymph Node Mapping. *Mol. Imaging* **2005**, *4*, 172–181.
34. Lakowicz, J. R. Radiative Decay Engineering: Biophysical and Biomedical Applications. *Anal. Biochem.* **2001**, *298*, 1–24.
35. Waldeck, D. H.; Alivisatos, A. P.; Harris, C. B. Nonradiative Damping of Molecular Electronic Excited States by Metal Surfaces. *Surf. Sci.* **1985**, *158*, 103–125.
36. Soller, T.; Ringler, M.; Wunderlich, M.; Klar, T. A.; Feldmann, J.; Josel, H.-P.; Markert, Y.; Nichtl, A.; Kurzinger, K. Radiative and Nonradiative Rates of Phosphors Attached to Gold Nanoparticles. *Nano Lett.* **2007**, *7*, 1941–1946.
37. Oldenburg, S. J.; Averitt, R. D.; Westcott, S. L.; Halas, N. J. Nanoengineering of Optical Resonances. *Chem. Phys. Lett.* **1998**, *288*, 243–247.
38. Stöber, W.; Fink, A.; Bohn, E. J. Controlled Growth of Monodisperse Silica Spheres in the Micron Size Range. *J. Colloid Interface Sci.* **1968**, *26*, 62–69.
39. Duff, D. G.; Baiker, A.; Edwards, P. P. A New Hydrosol of Gold Clusters. 1. Formation and Particle Size Variation. *Langmuir* **1993**, *9*, 2301–2309.
40. Sau, T. K.; Murphy, C. J. Seeded High Yield Synthesis of Short Au Nanorods in Aqueous Solution. *Langmuir* **2004**, *20*, 6414–6420.
41. Gulati, A.; Liao, H.; Hafner, J. H. Monitoring Gold Nanorod Synthesis by Localized Surface Plasmon Resonance. *J. Phys. Chem. B* **2006**, *110*, 22323–22327.